Digital Chemical Engineering 10 (2024) 100138

Contents lists available at ScienceDirect

Digital Chemical Engineering

journal homepage: www.elsevier.com/locate/dche

Original article

Model predictive control of an electrically-heated steam methane reformer

Berkay Çıtmacı [a], Xiaodong Cui [a], Fahim Abdullah [a], Derek Richard [a], Dominic Peters [a], Yifei Wang [a], Esther Hsu [a], Parth Chheda [a], Carlos G. Morales-Guio [a,*], Panagiotis D. Christofides [a,b,**]

[a] Department of Chemical and Biomolecular Engineering, University of California, Los Angeles, CA, 90095-1592, USA
[b] Department of Electrical and Computer Engineering, University of California, Los Angeles, CA 90095-1592, USA

ARTICLE INFO

Keywords:
Steam methane reforming
Experimental data modeling
Digitalization
Model predictive control (MPC)
Real-time control
Disturbance rejection

ABSTRACT

Steam methane reforming (SMR) is one of the most widely used hydrogen (H_2) production processes. In addition to its extensive utilization in industrial sectors, hydrogen is expanding it share as a clean energy carrier, and more sustainable and efficient H_2 production methods are continuously being explored and developed. One method replaces conventional fossil fuel-based heating with electrical heating through the flow of electrons across the reformer. At UCLA, an experimental setup was built of an electrically heated steam methane reforming process. This paper describes the system components, explains the digitalization of the experimental setup and introduces methods for building a first-principles-based dynamic process model using parameters estimated via data-driven methods from process experimental data. The modeling approach uses a lumped parameter approximation and employs algebraic equations to solve for gas-phase variables. The reaction parameters are calculated from steady-state experimental data, and the temperature change is modeled with respect to change in electric current using a first-order dynamic model. The overall dynamic process model is then used in a computational model predictive control (MPC) scheme to drive the process to a new H_2 production set-point under unperturbed and steam flowrate disturbance cases. The performance and robustness of the proposed MPC scheme are compared to the ones of a classical proportional–integral (PI) controller and are demonstrated to be superior in terms of closed-loop response, robustness, and constraint handling.

1. Introduction

Hydrogen (H_2) plays a fundamental role in the decarbonization and electrification of various industrial applications as a versatile and clean energy carrier (Ramachandran and Menon, 1998; Tarhan and Çil, 2021). It serves as a building block for the synthesis of ammonia (NH_3), methanol (CH_3OH), fertilizers and petrochemicals (Green, 1982). Industries are increasingly using H_2 as a fuel source for power generation, reducing greenhouse gas emissions, and promoting environmentally friendly practices. Hydrogen-powered vehicles, such as fuel cell electric vehicles, are emerging as an alternative to the battery-based electric vehicles in the transportation sector (Tanç et al., 2019). Industries like steel manufacturing utilize hydrogen in the reduction of iron ore, a process that offers a cleaner alternative to conventional methods, decreasing carbon emissions. This makes hydrogen an essential element in the pursuit of more sustainable metal production (Liu et al., 2021). Furthermore, the refining industry employs hydrogen extensively for desulfurization and hydrocracking processes (Choudhary and Saraf, 1975). These applications enhance the quality of fossil fuels and ensure compliance with environmental standards, which showcases the significance of H_2 in refining operations.

The industrial sector employs various methods to produce hydrogen, each tailored to specific needs and environmental considerations. Water electrolysis, is a clean and increasingly popular but energy intensive method that uses electricity to split water into hydrogen and oxygen. The rise of green hydrogen emphasizes the value of electrolysis powered by renewable energy sources, which also minimizes carbon emissions (Ursua et al., 2011). Thermochemical water splitting is also an emerging alternative that leverages high temperatures and chemical processes to release hydrogen from water or hydrogen-rich compounds (Safari and Dincer, 2020). The most widespread method for the production of hydrogen, however, is steam reforming, where a hydrocarbon or coal undergoes a chemical reaction with steam to generate hydrogen and carbon dioxide as schematically shown in Fig. 1(a) (Nikolaidis and Poullikkas, 2017). Natural gas steam reforming gives the

* Corresponding author.
** Corresponding author at: Department of Chemical and Biomolecular Engineering, University of California, Los Angeles, CA, 90095-1592, USA.
E-mail addresses: moralesguio@ucla.edu (C.G. Morales-Guio), pdc@seas.ucla.edu (P.D. Christofides).

https://doi.org/10.1016/j.dche.2023.100138
Received 7 December 2023; Received in revised form 23 December 2023; Accepted 23 December 2023
Available online 27 December 2023

highest yield of H_2 among hydrocarbons and coal. Methane is the molecule with the highest H:C molar ratio and the highest theoretical H_2 yield. The yields achieved in industrial hydrogen production are quite different from the maximum possible theoretical yields (Fig. 1(b)). This, however, is not due to a low degree of conversion but it is due to the fact that the large amount of energy needed to produce hydrogen is usually supplied by the raw material itself. Burning of natural gas to provide heat to the strongly endothermic steam reforming reaction, generates excess CO_2.

Among the different methods for industrial H_2 production, the most common is steam methane reforming (SMR), accounting for 48% of the total current hydrogen production (Uddin et al., 2020). Projections indicate that SMR will still be the most widespread H_2 production technique in 2050 (Uddin et al., 2020), particularly due to natural gas availability and the challenges with scaling up electrolyzer manufacturing to global scales (IEA, 2023). As industries prioritize sustainability, advancements in these production methods, coupled with innovations, are central in shaping a greener and more efficient future for hydrogen production within the industrial sector.

A sustainable enhancement to steam methane reforming involves substituting fossil fuel combustion with electricity to supply the necessary heat for the chemical reactions (Wismann et al., 2019). The use of renewable, carbon-free electricity to generate heat in an electric resistance-heated reformer promises to (i) displace natural gas combustion as a source of heat, (ii) deliver more compact, economic and efficient units for competitive H_2 manufacture, and (iii) increase H_2 yields per ton of natural gas while reducing its CO_2 emission intensity (Fig. 1(b)) (Perkin, 2000).

In an electrically heated SMR process, two electrodes are connected to the top and bottom of the tubular reactor with a washcoated catalyst, and an electric current is applied, resulting in a flow of electrons to generate heat. This flow of electrons results in a more uniform distribution of temperature in the radial direction, as shown in Fig. 1(a). In addition to electrically heated SMR, a novel method is introduced in Malerød-Fjeld et al. (2017) that leverages electric current for membrane separation of H_2. This process occurs within a proton-conducting membrane reactor, wherein the generated H_2 is extracted through a flow of electrons across a proton-permeable membrane. The real-time removal of H_2 changes the reaction thermodynamics to shift the equilibrium reactions towards more production of H_2 (Malerød-Fjeld et al., 2017). This increases the hydrocarbon conversion to 99%, which is around 74%–85% using conventional methods (Nikolaidis and Poullikkas, 2017). At UCLA, we have constructed an experimental setup for both electrically heated SMR and proton-conducting membrane reforming processes to further examine the reaction dynamics, and to develop modeling and control strategies while comparing these two technologies directly.

Model predictive control (MPC) plays a significant role in enhancing the efficiency and operability of industrial chemical processes, and could play a significant role in enhancing the efficiency and operability of steam methane reforming processes, particularly those connected to future electricity grids with high penetration of renewables. In SMR, where complex chemical reactions and heat transfer dynamics are tightly coupled, MPC will serve as a powerful tool for optimizing system performance. By using real-time measurements and predictive models, MPC can dynamically adjust operating parameters such as temperature, pressure, and inlet flow rates, to ensure optimal hydrogen production and minimize energy consumption. Although a great deal of work has been carried in the modeling and control of traditional fired SMR systems, significant knowledge gaps remain in the electrification of SMR reactors. For example, a computational study was conducted by Wu et al. (2017) using a robust CFD model for proposing an MPC for a traditional fired SMR process, and the results were compared to a PI controller. In Zecevic and Bolf (2020), a computationally efficient closed-loop system with a gain-scheduled MPC was introduced for a steam methane reformer, using a first-principle model for a fired reforming tube reactor to represent process dynamics. The gain-scheduled MPC, considering critical parameters such as outlet methane concentration and temperature, demonstrated adaptive operation, outperforming a PID controller and offering energy savings of 3%–5% (Zecevic and Bolf, 2020). This not only improved the overall process efficiency but also enabled better responses to disturbances and variations in operating conditions. The importance of MPC in SMR lies in its ability to increase yield and reduce energy costs, thereby contributing to the sustainability and economic viability of hydrogen production through steam methane reforming. It can be envisioned that MPC has an even bigger role to play in the implementation of future electrified SMR systems. In electrified systems, in addition to temperature, pressures, and flow rates, there is a need for the dynamic optimization of currents and voltages while ensuring the process operation to be within a safe operating regime. In this work, we present our preliminary efforts towards the construction, digitalization, modeling and control of an electrified steam methane reforming reactor. The key contribution is the development of a model and of a model predictive controller that uses the developed model and suitable constraints to achieve optimal closed-loop responses. The developed model and the controller can be solved fast and thus can be implemented in a practical setting.

2. Preliminaries

2.1. Nomenclature

Definitions of variables used in the modeling of the reactor:

- A_i: Pre-exponential factor for adsorption constant K_i of gas species i [Pa^{-1} for $i = CH_4, H_2, CO$ and unitless for $i = H_2O$]
- A_j: Pre-exponential factor for rate coefficient k_i for reaction j [mol $Pa^{0.5}$ (kg–cat s)$^{-1}$ for $j = 1$ (SMR reaction), mol (Pa kg–cat s)$^{-1}$ for $j = 2$ (WGS reaction)]
- C_i: Concentration of species i [mol m^{-3}]
- C_{p_i}: Specific heat capacity of gas species i [J (mol K)$^{-1}$]
- E_j: Activation energy for reaction j [J mol^{-1}]
- F: Total molar flow of gases [mol s^{-1}]
- F_i: Molar flow of gas species i [mol s^{-1}]
- K_i: Adsorption constant of gas species i [Pa^{-1} for $i = CH_4, H_2, CO$ and unitless for $i = H_2O$]
- K_j: Equilibrium constant for reaction j [Pa^2 for $j = 1$ (SMR reaction), unitless for $j = 2$ (WGS reaction)]
- k_j: Reaction rate constant of reaction j [mol $Pa^{0.5}$ (kg–cat s)$^{-1}$ for $j = 1$ (SMR reaction), mol (Pa kg–cat s)$^{-1}$ for $j = 2$ (WGS reaction)]
- P_i: Partial pressure of gas species i [Pa]
- q: Outlet volumetric flowrate [m^3 s^{-1}]
- q_i: Outlet volumetric flowrate of gas species i [m^3 s^{-1}]
- r_j: Rate of reaction for reaction j [mol (kg s)$^{-1}$]
- R: Universal gas constant [J (mol K)$^{-1}$]
- $\bar{R}$: Alloy tube resistance [Ohm]
- T: Reactor temperature [K]
- T_{p_i}: Temperature of inlet gas species i [K]
- T_s: Temperature of the surroundings [K]
- UA: Overall heat transfer coefficient times the heat transfer area [J (s K)$^{-1}$]
- V: Reactor volume [m^3]
- W: Catalyst weight [kg]
- ΔH_{r_j}: Heat of reaction j [J mol^{-1}]
- $\dot{m}_{p_i}$: Mass flow rate of gas species i [kg s^{-1}]
- ρ_i: Density of the gas species i in the reactor [kg m^{-3}]

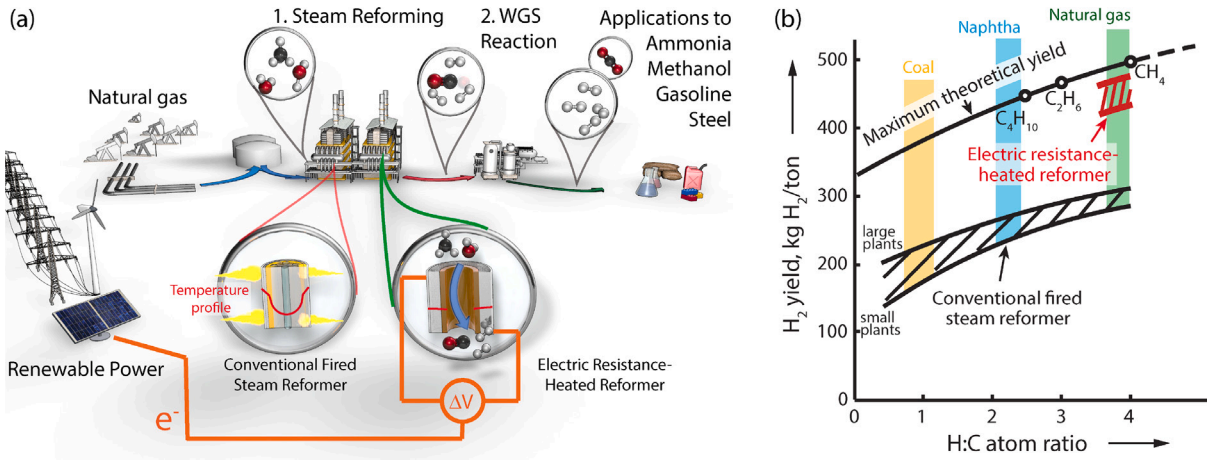

Fig. 1. (a) Schematic comparison of conventional fired steam methane reforming and electrically heated steam methane reforming. (b) Comparison of hydrogen production from hydrocarbons and coal for conventional fired and electric resistance-heated steam reformers.

2.2. Process overview

The overall goal of the joule-heating steam methane reforming process is to convert methane to produce emissions-free hydrogen gas in an electrically heated steam methane reformer. Instead of utilizing a conventional fossil fuel-based heating source, electrical heating is used in our work to heat up the reactor by applying an electric current directly through the reactor tube. In our experimental setup, methane, steam, and argon gases are flown into the reactor tube under certain temperature and pressure to react and produce hydrogen gas. The overall reaction can be demonstrated by the two independent reactions,

$$\text{Steam reforming}: CH_4 + H_2O \rightleftharpoons 3H_2 + CO, \qquad \Delta H_{298} = 206.1 \text{ kJ mol}^{-1} \tag{1a}$$

$$\text{Water gas shift}: CO + H_2O \rightleftharpoons CO_2 + H_2, \qquad \Delta H_{298} = -41.15 \text{ kJ mol}^{-1} \tag{1b}$$

The first reaction (Eq. (1a)) is the reforming reaction which converts methane and water to carbon monoxide and hydrogen. The second reaction (Eq. (1b)) is the water–gas shift reaction, which converts carbon monoxide and water to carbon dioxide and hydrogen gas. The overall reaction is endothermic due to the combination of a strongly endothermic reforming reaction and a slightly exothermic water-gas shift reaction. In general, the intrinsic reaction kinetics and mass transport phenomena occurring in the reactor need to be considered when determining the reactor dynamics. In this work, we focus more on the reaction kinetics since the internal and external diffusion resistances of catalyst particles does not appear in the intrinsic reaction rates. Considering the reaction kinetics, the rate determining step is the activation of methane, since it has a stable structure that demands higher energy to break the C–H bond (Wei and Iglesia, 2004a,b,c,d,e,f). In order to catalyze the activation of methane in our experiment, a highly active Ni-based catalyst is used. Furthermore, the experiment is also performed under a high temperature to overcome the energy barrier and increase the reaction rates.

The electrical heating provides a radially near-uniform heat supply with a very small temperature gradient that helps to prevent carbon formation by keeping the gas temperature close to the equilibrium temperature (Wismann et al., 2019). Also, the temperature gradient between the inner and outer wall of the reactor is very small in contrast to burner-heated reactors, which helps to reduce the thermal stress and extends reactor lifetime (Wismann et al., 2019). This also means that the thermal gradient across the washcoated catalyst is very small, which improves the catalyst utilization. Wismann et al. (2019) also suggests that electrically heated SMR reactors can reach the same conversion as industrial burner-heated tubular reformers, but with a reactor volume up to 100 times smaller.

The reactions shown in Eq. (1) are complex reactions, as they are parallel in H_2O and series in CO. Furthermore, all the reactants and products are in gas phase. As a result, modeling the reaction kinetics for this system is inherently challenging since, due to the presence of complex reactions, the conversion cannot be used for modeling. In our simulations, the concentrations of hydrogen, methane, water vapor, carbon dioxide, carbon monoxide, and argon are the outputs that depend on the current flowing thorough the reactor, and the current is manipulated to adjust the temperature of the reactor. Prior to the experiment, pure H_2 at high temperature is flown through the tubular reactor to activate the nickel catalyst. Following the H_2 flow, Ar is flown to remove the excess hydrogen remaining in the system before CH_4 and steam are flown. The experimental process flow diagram is shown in Fig. 2.

We built an experimental steam methane reforming setup at UCLA, whose details are presented in Richard (2021). A similar setup was built by Wismann et al. (2019) and a series of experiments were conducted to understand the concentration and temperature distribution better inside the reactor. In our work, we initially focus on the development of a nonlinear first-principles-based model that incorporates kinetic rate parameters extracted from experimental data obtained from our experimental reactor. This model is subsequently used in the present work for the development and evaluation via numerical simulations of a model predictive controller. Eventually, we aim to experimentally implement the model predictive controller to control the joule-heated SMR reactor. Our longer term goal is to use these models as a starting point to build controllers for the more complex process of SMR in a proton membrane reactor setup (where hydrogen production via SMR and hydrogen removal via a proton membrane occur in the same unit) in our laboratory.

3. Digitalization of the experimental setup

In this section, we present the digitalization of the experimental reactor, which is an integral part of measurement sensor data collection and control action implementation. Specifically, the data collected via the digitalized experimental setup described below is used to fit the model parameters for the dynamic model used in MPC.

3.1. Overview

An experimental setup is built at UCLA for two steam methane reforming reactors. This experimental setup makes it possible to conduct experiments with a proton membrane reactor and a joule heating

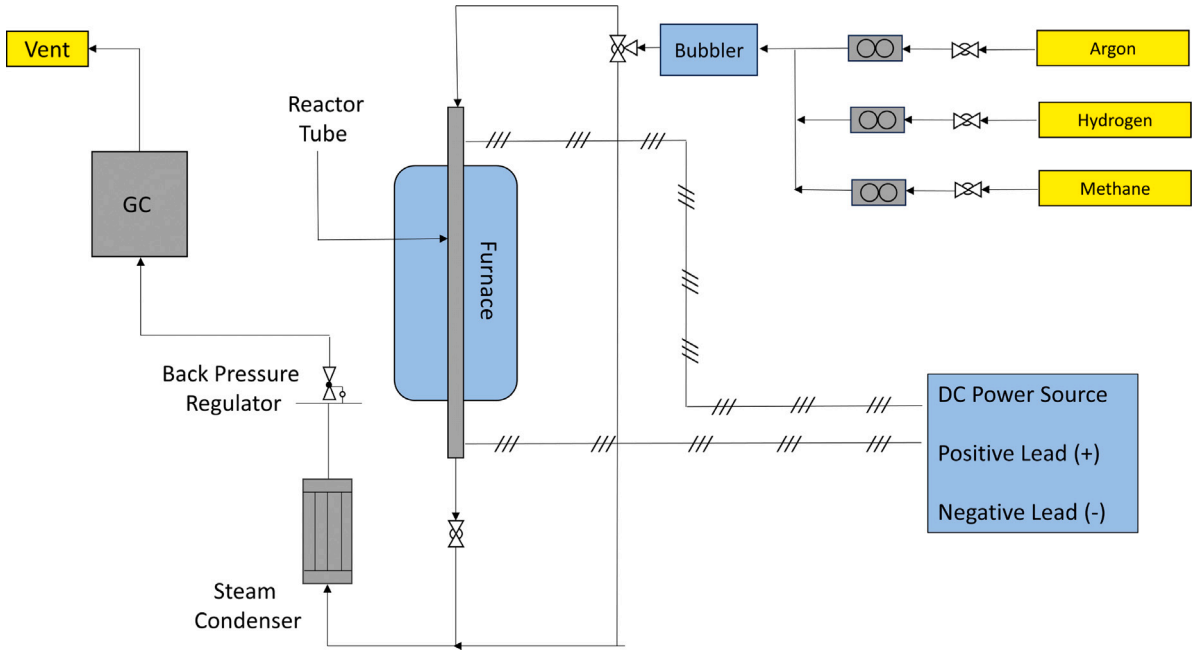

Fig. 2. Process flow diagram for experimental joule-heating steam methane reforming process.

steam methane reformer. Both reactor outlets can be quantified using a gas chromatograph. The inlet flow gases can be directed to either of the processes by arranging the valve configuration. This study focuses on electrically heated steam methane reforming. The majority of the lab equipment for both processes are common. The main difference between both processes is the source of applied potential. The proton membrane reactor uses a potentiostat (Metrohm 302N) to adjust the current flowing through the reactor for separation of hydrogen through a $BaZr_{0.8-x-y}Ce_xY_yO_{3-\sigma}$ (BCZY) membrane while the joule-heating setup uses a power supply to flow current to heat up the reactor, replacing fossil fuel-based heating (Richard, 2023). The experimental setup at UCLA is shown in Fig. 3.

Both setups are digitalized through a connection to a common Laboratory Virtual Instrument Engineering Workbench (LabVIEW) interface. Through LabVIEW, it is possible to manipulate actuators and read data from the sensors in real time. The previous experience with LabVIEW for the electrochemical CO_2 reduction reactor discussed in Çıtmacı et al. (2022) considerably accelerated the building of the new interface. It is possible to collect data and perform real-time control with the experimental steam methane reforming setups through LabVIEW.

3.2. Sensors and actuators

The experimental setup involves constant change of parameters such as temperature, pressure, current, etc. In order to measure these changes, multiple sensors, including thermocouples (Omega K-type) and pressure transducers (Omega PX359 - 1KAI), were installed. There are three thermocouples in the system. The first is placed in the middle of the wall on the joule-heated tubular reactor. The second is placed on the inside the steam box. The third one is placed on the wall of the gas flow pipe that is right before the inlet to the reactor.

There is one pressure transducer used for the joule-heated steam methane reforming process, which measures the pressure of the flow system. This pressure can be adjusted and kept constant through back pressure regulators (Equilibar) attached to the system. The aforementioned thermocouples, pressure transducers, and back pressure regulators are digitalized through a National Instruments Compact Rio. A Compact Rio is a reconfigurable, industrial grade data collection system that can work with LabVIEW.

The gas flowrates are set through MKS mass flow controllers (MFC) controlled by MKS 946 Vacuum system controller. It is possible to set flowrates for 5 gases, and the unit is standard cubic centimeters per minute (sccm). The MFCs are also connected to the LabVIEW interface and their set-point can be changed in real time.

The SMR system is equipped with two steam generators that supply steady inlet streams of water vapor to the joule heating and proton membrane reactors. Each steam box houses a bubbler encased within fiberglass thermal insulation. Using a K-type thermocouple, an Arcon temperature actuator, and electrical heating tape, a bubbler is set to a desired steam-to-carbon (s/c) ratio via temperature control. At a specific water temperature, the Antoine equation provides the vapor pressure of steam in the bubbler which is effectively the partial pressure of steam in the inlet gas mixture. The temperature sensor and Arcon actuator amount to PI control over the thermodynamic equilibrium of the inlet gas mixture and liquid water phase in each of the bubblers.

The tubular reactor is the main component of the joule-heated SMR setup. The tubular reactor is shown in Fig. 4. The reactor tube (Goodfellow Corporation: 72.8% Fe, 22% Cr, 5% Al, 0.1% Y, and %0.1 Zr alloy) has a length of 500 mm, an outer diameter of 6 mm, an inner diameter of 5.4 mm, and is wrapped in a fiberglass based insulation layer to prevent heat losses (not shown in Fig. 4) (Richard, 2021, 2023). In addition to this layer, there is an insulation furnace (Applied Test Systems, 321C-75-8-12) around the reactor tube. The furnace has a ceramic foam material as an extra layer of insulation. The furnace is used to provide thermal insulation only for these experiments and was not used to provide heat. Power cables from the power supply are connected to each end of the reactor tube. Using the power supply a potential is applied across the axial direction of the reactor driving a current through the metal tube. In this configuration, heat is uniformly generated along the length of the tube by the passage of electrons through the resistive metal reactor tube. The power supply shown in Fig. 5. A Chroma programmable DC power supply (62012P-40-120) is the main actuator in the experimental setup. It is connected to the LabVIEW interface through a driver provided by the manufacturer. It is possible to set the applied potential through the power cords. It is also possible to set a current set-point, and the power supply will accordingly adjust the applied potential to obtain the given current set-point. To control the joule-heating SMR setup, the power supply

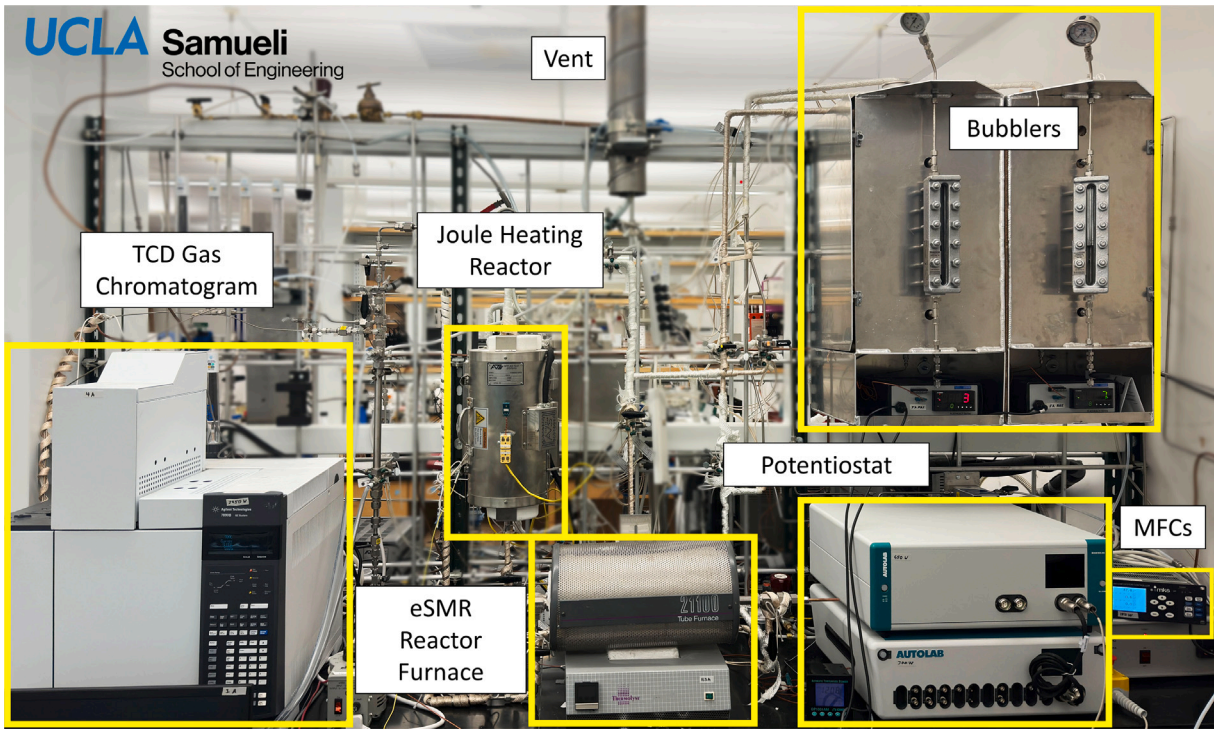

Fig. 3. Experimental setup for steam methane reforming processes at UCLA.

can adjust the current flowing through the reactor to provide the heat necessary for the reactions.

Fabrication of the washcoated reactor tubes (procedure with which catalyst is deposited on the tube walls) began with pretreatment of the FeCr Alloy tube followed by application of the coating in a multi-step process. Pretreatment was conducted by running a gentle flow of air through the tube while being heat treated at 950 °C for 10 h. The purpose of the pretreatment was to form a uniform oxide layer on the surface of the tube for the washcoat to adhere to. All high temperature changes including pretreat and calcination used a ramp rate of 1.4 °C to prevent crack formation in the washcoat or oxide layer. After pretreatment, Zr powder was mixed with 20 mL of deionized water whose pH was adjusted to 10 by adding a drop of 25% aqueous ammonium hydroxide. The solution was mixed with a magnetic stir bar at 300 rpm for 30 min, followed by bath sonication for 20 min. Immediately after sonication, the slurry was inserted into the tube using a pipet until the tube was filled. The tube was oriented vertically and plugged at the bottom with a nipple designed to slowly release the liquid upon applying a slight pressure inside the tube. Once filled, a syringe pump was attached to the top of the tube with a Swagelok fitting. The syringe pump forced a controlled 20 ml min^{-1} flowrate of air into the top of the tube, forcing the slurry to drain through the nipple at a steady rate. A total of 50 ml of air was forced through the tube in this way to ensure all excess slurry was drained. Coated tubes were dried at 110 °C for 1 h before calcination at 500 °C for 1 h. Multiple layers were added to achieve the desired loading by repeating the process just described. Catalyst addition was done by wet impregnation of the washcoat using a solution of 10 g of nickel nitrate hexahydrate dissolved in 15 ml of deionized water. Similar to how the washcoat was applied, the impregnation solution was added to the tube and allowed to set for at least 1 min to allow the solution to fill the pores in the washcoat. The solution was drained, and air was gently blown through the tube to remove excess solution. After air drying for 1 h, the tube was dried at 110 °C for 1 h followed by calcination at 500 °C for 1 h. By this technique, a stable washcoat was obtained with a total washcoat loading of 39.8 mg.

An Agilent Technologies 7890B gas chromatogram is used to measure the gas phase products in real-time. A thermal conductivity detector (TCD) is used to quantify each gas product. The product gases first go through a condenser to separate water vapor from the remaining gas products. After condensing the steam, H_2, CO_2, CO, and unreacted CH_4 flows into the GC. It takes 15 min for each gas sample analysis. Then, it takes 3 min to cool down the GC for a new injection. Thus, the GC can take one gas sample every 18 min.

In our setup, the GC measurements are initiated automatically using an external Python code. The main algorithm behind automated GC analysis is described in Çıtmacı et al. (2022). After each GC run is finalized, the results are automatically processed by calculating the areas underneath each gas species peak and comparing it to previously calibrated peaks for each gas. An example of GC peaks is shown in Fig. 6.

Remark 1. The calculation of the concentrations from the GC analysis are delayed by 15 min. This situation is a challenge for dynamic processes. However, the present work only uses steady state experiments to evaluate the reaction kinetics parameters.

3.3. Smart manufacturing innovation platform connection

The LabVIEW interface is connected to Smart Manufacturing Institute's (CESMII) Innovation platform (SMIP). All the data generated from the setup is sent to the platform securely through the query language GraphQL (Hartig and Pérez, 2018). The profile for the SMR system is shown in Fig. 7. It is organized and hierarchical; all the attributes are defined under the equipment and each attribute has endpoints to store relevant data.

SMIP will also be used to implement a model predictive controller scheme in the future. Luo et al. (2023) demonstrated the use of SMIP in real time control by transferring data between the lab computer operating LabVIEW and another computer with solver licenses. Thus, SMIP is planned to play a key role in implementing the MPC designed in this computational paper on the experimental setup.

Fig. 4. Reactor tube and insulation furnace.

Fig. 5. Power supply connected to the tubular reactor for electrical heating.

4. First-principles modeling

The SMR system is challenging to model due to the complex nature of the SMR reactions, all species being in gas phase, transfer phenomena in the reactor, and spatio-temporal variations in the tubular reactor giving rise to partial differential equations. Due to these challenges, the tubular reactor is generally modeled with CFD simulations, which are computationally expensive and not practical to use for real-time predictive control (Mokheimer et al., 2015; Lao et al., 2016). Latham et al. (2011) modeled the SMR process as a burner-heated 1-dimensional

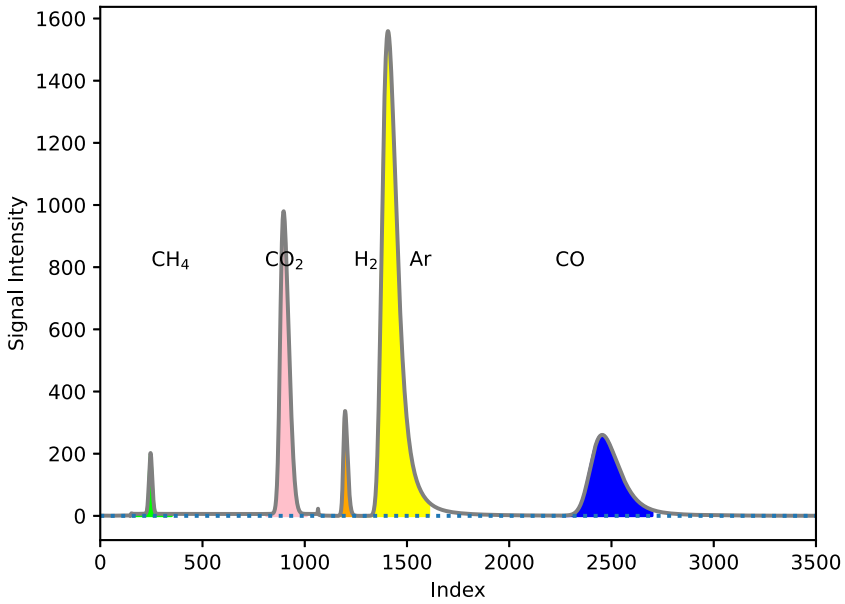

Fig. 6. Gas chromatogram peaks for quantifying the gas phase products.

fixed-bed tubular reactor surrounded by a large-scale furnace using first-principles model equations and industrial data for online deployment of the model. The radiative heat transfer was modeled using temperature from various locations on the tube in conjunction with the Hottel zone method. As the scale of the process setup gets larger, the effects of the transport phenomena becomes more important. In this work, we propose a simplified modeling approach that can be used for a small scale experimental reactor and can be implemented in real-time for predictive control. To this end, the modeling options for approximating the tubular reactor as a continuously stirred tank reactor (CSTR) are explored.

The first-principles model is based on the mole balance of each species in a CSTR. However, compared to a liquid phase CSTR, the gas phase CSTR is harder to model using first principles because the volumetric flow rate changes with reactions due to the gas phase stoichiometry change after reactions. The reactor is operated at 1 bar and between 600–1000 °C. Due to low pressure and high temperature conditions, the ideal gas law is assumed to hold. As a result, in the reactor, $PV = nRT$ must hold at all times, where P is the pressure, and n is the total number of moles. Also, since the experimental setup is a flow system, $Pq = FRT$ must also hold for the flow calculations, where q is the volumetric flowrate and F is the molar flowrate.

Eq. (2) demonstrates the equations used for the calculation of the reaction rates. The kinetic parameters and mechanism are taken from Xu and Froment (1989) and Abbas et al. (2017). Each species has an adsorption coefficient that is a function of temperature. The reaction rates are written in terms of partial pressures due to them occurring in the gas phase.

$$r_{1,SMR} = \frac{k_1}{P_{H_2}^{2.5}} \cdot \frac{P_{CH_4} \cdot P_{H_2O} - \frac{P_{H_2}^3 \cdot P_{CO}}{K_1}}{(DEN)^2} \tag{2a}$$

$$r_{2,WGS} = \frac{k_2}{P_{H_2}} \cdot \frac{P_{CO} \cdot P_{H_2O} - \frac{P_{H_2} \cdot P_{CO_2}}{K_2}}{(DEN)^2} \tag{2b}$$

$$DEN = 1 + K_{CO} \cdot P_{CO} + K_{H_2} \cdot P_{H_2} + K_{CH_4} \cdot P_{CH_4} + K_{H_2O} \cdot \frac{P_{H_2O}}{P_{H_2}} \tag{2c}$$

$$k_j = A_j \cdot \exp\left(-\frac{E_j}{R \cdot T}\right), \quad j = 1, 2 \tag{2d}$$

$$K_i = A_i \cdot \exp\left(-\frac{\Delta H_i}{R \cdot T}\right), \quad i = CH_4, H_2O, CO, H_2 \tag{2e}$$

In order to model the reactor as a lumped parameter system, it is necessary to write the mass balance equations for each gas. This generates 6 nonlinear ordinary differential equations, as shown in Eq. (3). Additionally, since the reaction rates are functions of temperature, it is necessary to have an energy balance, which will be discussed in Section 5.2.

$$\frac{dC_{CH_4}}{dt} = \frac{1}{V_R}\left(F_{CH_4,0} - r_1 \cdot W - q \cdot C_{CH_4}\right) \tag{3a}$$

$$\frac{dC_{H_2O}}{dt} = \frac{1}{V_R}\left(F_{H_2O,0} - (r_1 + r_2) \cdot W - q \cdot C_{H_2O}\right) \tag{3b}$$

$$\frac{dC_{CO}}{dt} = \frac{1}{V_R}\left((r_1 - r_2) \cdot W - q \cdot C_{CO}\right) \tag{3c}$$

$$\frac{dC_{H_2}}{dt} = \frac{1}{V_R}\left(F_{H_2,0} + (3 \cdot r_1 + r_2) \cdot W - q \cdot C_{H_2}\right) \tag{3d}$$

$$\frac{dC_{CO_2}}{dt} = \frac{1}{V_R}\left(r_2 \cdot W - q \cdot C_{CO_2}\right) \tag{3e}$$

$$\frac{dC_{Ar}}{dt} = \frac{1}{V_R}\left(F_{Ar,0} - q \cdot C_{Ar}\right) \tag{3f}$$

where $F_{i,0}$ is the inlet molar flowrate of species i.

Remark 2. In the experiment, a relatively short, in terms of axial length, reactor and good thermal insulation are used. Therefore, a lumped parameter system behavior is assumed when the first-principles model is derived, which means there is no spatial variation in temperature and concentration inside the reactor taken into account in the model development. Furthermore, the reaction is expected to consume more heat in the inlet section of the tubular reactor (Wismann et al., 2019), indicating that most of the conversion occurs near the reactor inlet and, for the remainder of the tube, the temperature and concentration profiles do not vary significantly in the axial direction, thereby justifying further the use of a lumped parameter modeling approach.

4.1. Constant pressure and temperature case

The constant pressure and temperature case is considered as a starting point. In this case, the total concentration in the reactor, C_T, is constant according to the ideal gas law,

$$C_T = C_{CH_4} + C_{H_2O} + C_{CO} + C_{H_2} + C_{CO_2} + C_{Ar} = \frac{P}{RT} \tag{4}$$

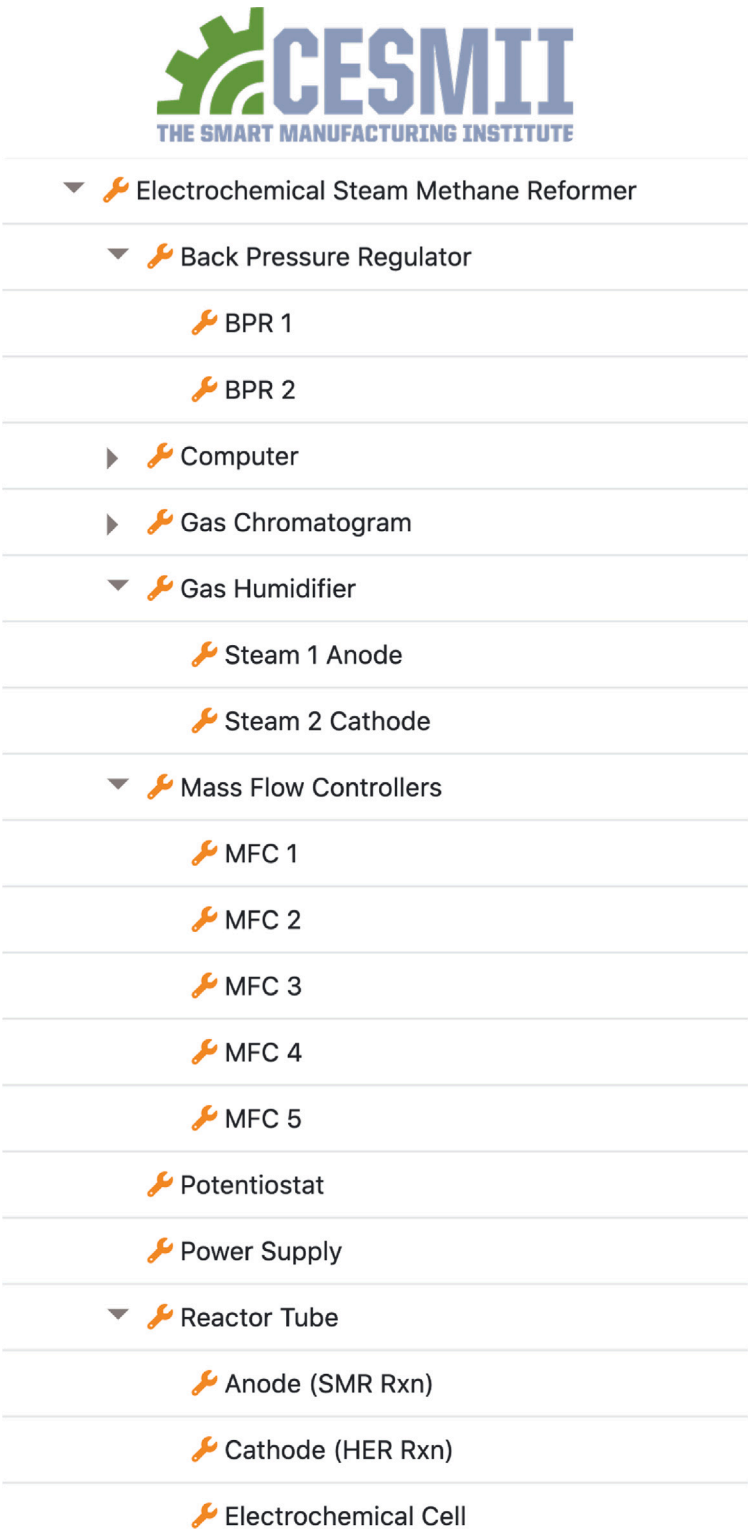

Fig. 7. The SMR system profile on SMIP.

Due to the species being in gas phase, the outlet volumetric flowrate, q, is a function of temperature and cannot be assumed constant for all temperatures. Since q appears as a new variable, one new equation should be introduced, which is Eq. (4). This equation originates from the ideal gas law since $C_T = F/q$, where F is the total outlet molar flow rate, and indicates that the total gas concentration in the reactor is a function of only temperature and pressure. As a result, the total concentration inside the reactor does not change under constant temperature and pressure, and its differential with respect to time can be set to zero as follows:

$$\frac{dC_T}{dt} = \frac{dC_{CH_4}}{dt} + \frac{dC_{H_2O}}{dt} + \frac{dC_{CO}}{dt} + \frac{dC_{H_2}}{dt} + \frac{dC_{CO_2}}{dt} + \frac{dC_{Ar}}{dt} = 0 \quad (5)$$

where the differentiation of the total concentration term is written as the summation of concentration differentials with respect to time

for each of the 6 gas species, which are already written explicitly in Eq. (3). Substituting the individual species' mass balances into Eq. (5), we obtain the relation,

$$\frac{dC_T}{dt} = \frac{1}{V_R}\left(F_{CH_4,0} + F_{H_2O,0} + F_{H_2,0} + F_{Ar,0} + 2r_1\ W - qC_T\right) \tag{6}$$

whose right-hand side can be equated to zero to yield

$$F_{T0} + 2r_1\ W = q\frac{P}{RT} \tag{7}$$

from which the final expression for the outlet volumetric flow rate can be obtained as

$$q = \frac{F_{T0} + 2r_1 W}{\frac{P}{RT}} \tag{8}$$

This equation shows that the outlet flowrate is a function of the reforming reaction rate. After replacing all occurrences of q in Eq. (3) by Eq. (8), the system of differential equations for constant temperature can be solved with numerical integration and then compared via experimental results. In the experimental setup, the constant temperature and pressure conditions can be achieved by controlling the power supply to regulate temperature through current and using pressure regulators.

4.2. Variable temperature case

The SMR reactor can be heated by electricity. Specifically, the current across the reactor can be manipulated to heat the reactor tube, which will change the temperature of the reactor. A higher temperature can produce a higher amount of hydrogen and increase methane conversion. Hence, it is necessary to derive the dynamic model of the case with variations in temperature. However, in this case, the total concentration changes according to the change in temperature. Therefore, the expression of the volumetric flow rate also changes and now depends on the derivative of the temperature with respect to time. The derivation of the expression for the outlet volumetric flow rate is done for the temperature-varying case using the same steps as Eqs. (4)–(8) and shown in Eq. (9).

$$\frac{dC_T}{dt} = -\frac{1}{T^2}\cdot\frac{P}{R}\cdot\frac{dT}{dt} \tag{9a}$$

$$\frac{dC_T}{dt} = \frac{1}{V_R}\cdot\left(F_{T,0} + 2\cdot r_1\cdot W - q\cdot C_T\right) \tag{9b}$$

$$\frac{dT}{dt} = T^2\cdot\frac{R}{P}\cdot\frac{1}{V_R}\cdot\left(q\cdot\frac{P}{R\cdot T} - F_{T0} + 2\cdot r_1\cdot W\right) \tag{9c}$$

$$q = \frac{F_{T0} + 2\cdot r_1\cdot W}{\frac{P}{RT}} + \frac{V_R}{T}\cdot\frac{dT}{dt} \tag{9d}$$

4.3. Steady state simulation and comparison with experimental results

The steady state simulation results at different temperatures are shown in Fig. 9. When the temperature is below approximately 600 °C, the volumetric flows for hydrogen and methane going out of the reactor remain constant, which means there is nearly no reaction. When the temperature is higher than 600 °C, the hydrogen volumetric flow rate starts to increase, and the methane volumetric flow rate starts to decrease. The reason behind this phenomenon is that the reaction rate increases with the increase of temperature.

Remark 3. In the constant temperature and pressure case, the time to reach the steady state is below 10 s, indicating extremely fast dynamics.

5. Model parameter estimation using experimental data

5.1. Reaction kinetics estimation

Steam methane reforming reaction mechanisms are taken from Xu and Froment (1989). However, the catalyst used in Xu and Froment (1989) is different from the catalyst used in our experimental study. As a result, the reaction parameters presented in Xu and Froment (1989) are not expected to be the same as those in our experiments. The preparation of the catalyst will also impact the distribution of the active sites and the reaction kinetics. Thus, the first step towards modeling the system is to estimate the parameter values in our specific setup.

As discussed in Section 4, this experimental setup is modeled as a continuous stirred tank reactor (CSTR; lumped parameter modeling). Using the concentrations at steady state, the lumped parameter model is compared to the experimental observations for gases. The activation energies presented in Xu and Froment (1989) for reforming and water–gas shift reactions were re-calculated to align closely with our experimental concentrations. The comparison between the experimental data and the model calculations after adjusting the activation energy of the reforming reaction is shown on Fig. 9. An optimization problem was established to minimize the difference between calculated pre-exponential factors and activation energies, such that the steady states of the dynamic model corresponded to experimental measurements. After solving the optimization problem, the pre-exponential factors and activation energies for the reforming reaction are found to be $4.22\cdot10^{16}$ mol $Pa^{0.5}$ (kg–cat s)$^{-1}$ and 384.5 kJ/mol respectively, and for the water–gas reaction are found to be $4.22\cdot10^{7}$ mol Pa (kg–cat s)$^{-1}$ and 128.9 kJ/mol, respectively.

Remark 4. Due to the nonlinearity of the optimization problem, different solvers may find different solutions corresponding to different local optima. In our case, the best fit that gives the closest alignment with the experimental data among various Python library $SciPy$ solvers is taken to be the final estimate of the parameters. Following this methodology, the least-squares sequential quadratic programming method was used as the final optimization solver.

Remark 5. Wismann et al. (2019) suggests that the temperature difference between the inlet region and the outlet region of the reactor may reach up to 300 °C. Our approach approximates the tubular reactor as a lumped parameter system and does not account for the spatial temperature gradient. This approach will be improved by modeling with multiple lumped parameter models in series that will use the temperature values from multiple thermocouple sensors attached to the tubular reactor. The reaction kinetic parameters will be calculated accordingly.

5.2. Temperature dependence with respect to time

As described in Section 4.2, the system of differential equations needs to include one equation for the energy balance. This energy balance can be approximated as follows:

$$\frac{dT}{dt} = \frac{I^2\bar{R} + \sum_i \dot{m}_{p_i}C_{p_i}(T_{p_i} - T) - Wr_{SMR}\Delta H_{SMR}(T) - Wr_{WGS}\Delta H_{WGS}(T) + UA(T_s - T)}{\sum_i \rho_i C_{p_i} V} \tag{10}$$

The detailed energy balance of Eq. (10) is a modified version of the energy balance presented in Fogler (2005), adapted for electrically heated steam methane reforming. The heat input is replaced by $I^2\bar{R}$, which is the power supplied by the flow of electrons. This equation requires further experiments to estimate the value of the heat transfer coefficient (U), as well as the coefficients for radiant and convective heat losses to the environment. Determining these parameters requires a much larger experimental data set and is not feasible with the current data set, which is reserved to determine the key model parameters related to reaction kinetics. The lack of knowledge of these parameters in Eq. (10) renders it unusable in practice until further experimental data is available. The temperature change with respect to time is instead approximated using the available experimental data by fitting

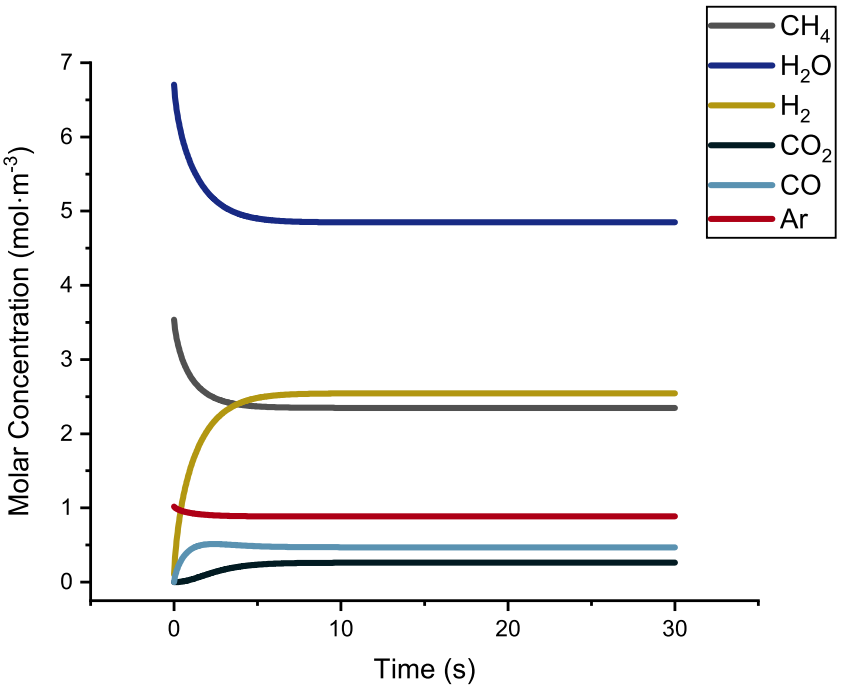

Fig. 8. Open loop dynamic evolution based on first-principles dynamic model equations under constant temperature (800 °C), constant current (40 A) and constant pressure (1 bar).

the data of current and temperature vs time to a first-order dynamic model. The derivation of such a first-order model is shown in Eq. (11), starting from the Laplace domain and its transition to time domain.

$$\frac{T'(s)}{I'(s)} = \frac{K}{\tau s + 1} \tag{11a}$$

$$T'(s) = \frac{K}{\tau s + 1} \cdot I'(s) \tag{11b}$$

$$T'(t) = I'(t) \cdot K \cdot (1 - \mathrm{e}^{-t/\tau}) \tag{11c}$$

$T'(s)$ and $I'(s)$ are the deviation form notations for temperature and current, respectively, while K and τ are the process gain and time constant, respectively. If the K and τ values can be extracted from the experimental setup by fitting the temperature dynamics following a step change in the current, the time-derivative of the temperature can be written as

$$\frac{\mathrm{d}T}{\mathrm{d}t} = -\frac{T - T_s}{\tau} + K \cdot \frac{I - I_s}{\tau} \tag{12}$$

where T_s and I_s are the initial steady-state values. Eq. (12), though approximate, is sufficiently accurate when its parameters are calculated via experimental data and, in this work, is used in lieu of Eq. (10). With this approach, the reaction heat generation, power supply efficiency, and heat transfer coefficients are accounted for in the dynamic behavior approximation via K and τ. In order to estimate the values of K and τ, it is necessary to apply a step change in current and record the dynamic behavior of the temperature. Thus, when the current was at 32 A, and the system was at steady state, the current was reduced to 0 A while the system was active, and the corresponding data shown in Fig. 10 was collected. In addition to this, steady state temperature values are recorded at various currents, and the data is shown in Fig. 11. We note here that, as seen in Figs. 10 and 12, the dynamics of the SMR are fast, with steady states being reached in under 2000 s, which justified the use of only steady-state data for identification of the kinetic parameters. In particular, since the GC measurements are only available every 18 min (1080 s), even if transient data were to be used, only a maximum of two extra data points per run could be used (e.g., at times 1 s, 1081 s, 2161 s, with the first two readings being additional transient measurements, and the last reading corresponding to the currently used steady-state measurement). Hence, the transient data was not used in the kinetic parameter estimation in this work.

The data shown in Eq. 10 is fitted to a first-order model of the form of Eq. (11c) to get the process gain (K) and process time constant (τ) values, which were calculated to be 14.54 K/A and 284 s, respectively. As the temperature change occurs immediately following the change in the current, no dead time was considered in the first-order model form. The first-order model fit and experimental variation of the temperature with respect to the step change in current are compared in Fig. 12.

Remark 6. The step change in current is aimed to be large to capture a broader range of temperature change. However, to avoid harming the catalyst morphology, the change is made in the cooling direction since rapid, large increases in the temperature are detrimental to the catalyst.

Remark 7. Fig. 11 demonstrates that the relation between steady-state current and temperature is a second order polynomial and mildly nonlinear. The approach mentioned in this section is for first-order linear processes, limiting the approach to a specific temperature regime. However, since the temperatures in the current simulations remain close to the range of 800 °C to 900 °C, the K and τ values of 14.54 K/A and 284 s, respectively, work adequately. If a different temperature regime is targeted for operation in a future work, the K and τ values can be re-calculated based on data from the new regime. However, since the goal is to eventually use Eq. (10) instead of Eq. (12), this limitation will likely not be a concern in future works once Eq. (10) can be used. In the current work, this limitation does not manifest due to the results being obtained for the specific temperature range studied. However, in future works, the model of the temperature dynamics can be improved with an incorporation of other first-order models for higher temperature ranges or can be replaced entirely by a data-driven model, such as a recurrent neural network. This would also account for the altered reaction dynamics at higher temperature regimes.

Remark 8. The first-order model will be valid for a specific inlet flow of CH_4. The amount of CH_4 in the inlet is pivotal for the reaction

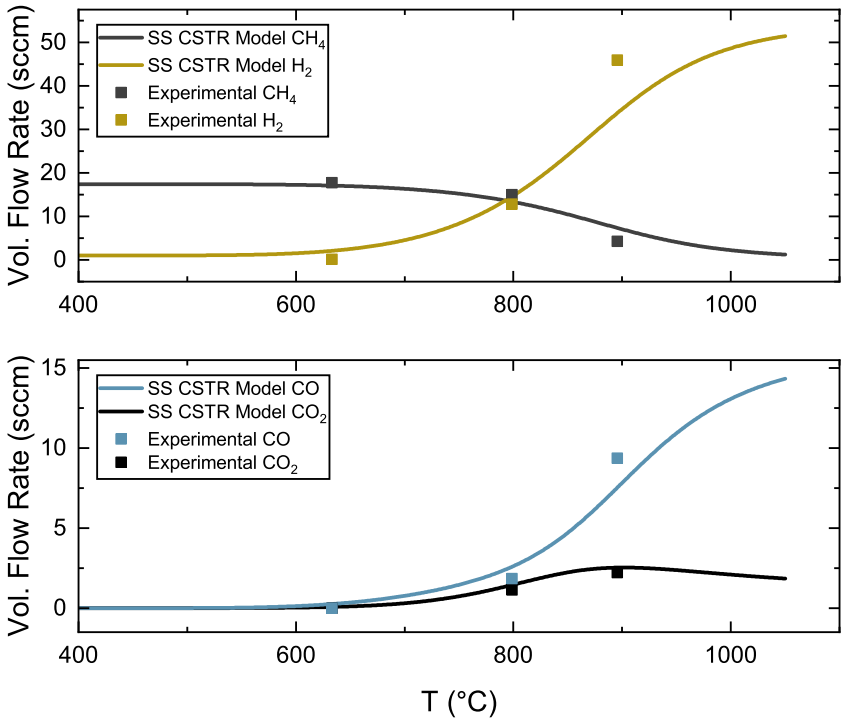

Fig. 9. Comparison of lumped parameter model steady-state with experimental observations.

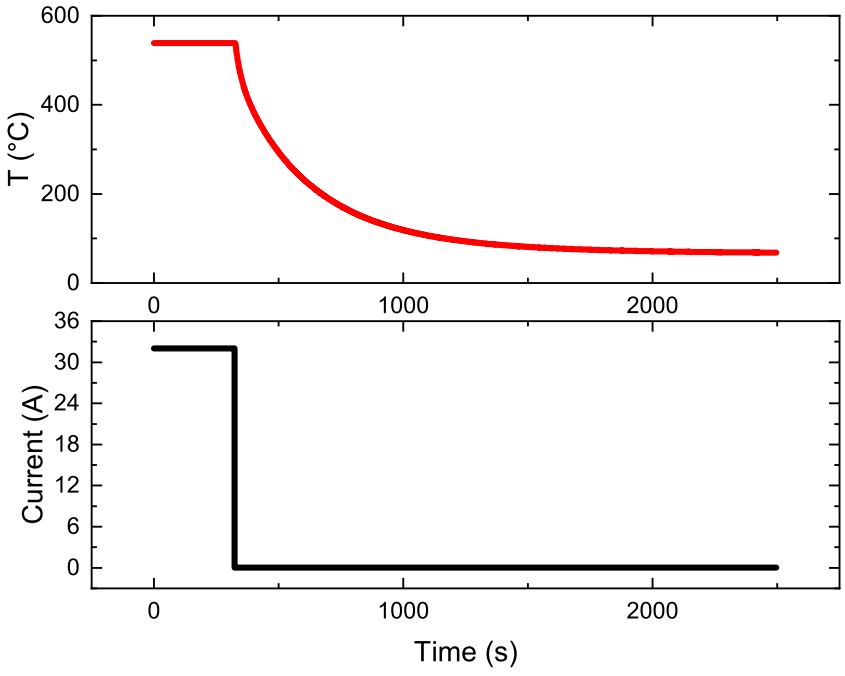

Fig. 10. Dynamic change in temperature with respect to a step change in current.

kinetics. Thus, the first-order model parameters should be calculated for various CH_4 inlet conditions for a more comprehensive model. Specifically, the parameters K and τ in the first-order model will be slightly different for each inlet flow of CH_4. Hence, from numerous experiments at different flow rates of CH_4, K and τ can be calculated and stored in a table. Since, in the experiment, the inlet flow of CH_4 is usually constant throughout the experiment, for a specific experiment, the corresponding values of K and τ can be determined from the table and used for the first-order model. If the CH_4 flow rate does change during the experiment, the values of K and τ should be updated based on the table. However, once the unknown parameters for Eq. (10) are determined, the first-order model will no longer be used, and the full energy balance of Eq. (10), which accounts for all variables including inlet flow of CH_4, will be used instead; this approach will be pursued in a future work.

6. Feedback control

Our work aims to build a feedback control architecture for the experimental SMR setup that is robust to disturbances. It is possible to

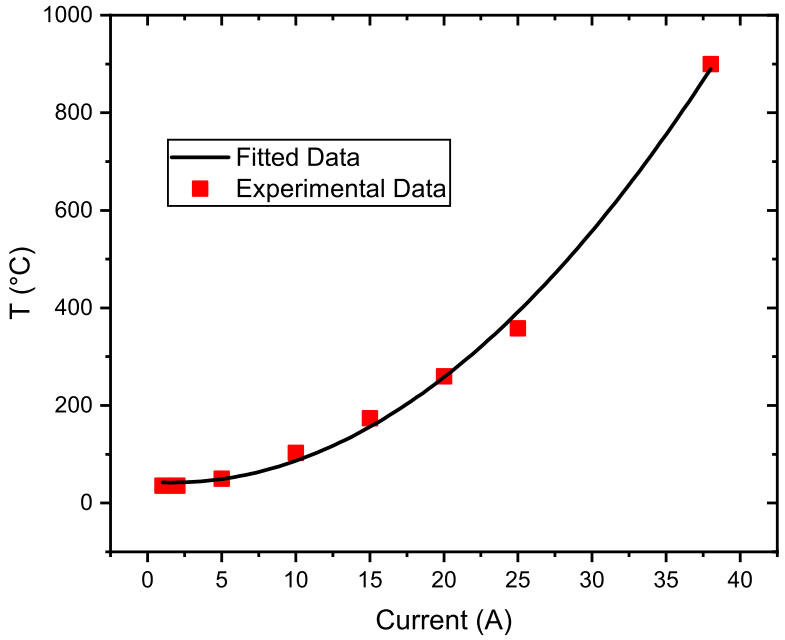

Fig. 11. Temperature values against current set-points at steady state.

decide the best controlling strategies by accounting for the limitations of the process, since first-principles and data-driven dynamic temperature variation models are available to simulate the experimental behavior. For this purpose, a PI control scheme is compared to a model predictive controller because a PI controller is the classical feedback controller that would typically be used in the absence of advanced model-based controllers such as MPC. In the following simulations, the pressure is assumed to be constant at 1 bar, while the temperature is varied to regulate the reaction rates to drive the H_2 production. The implementation of the constant pressure in the experimental setup in future work will be realized by using a back pressure regulator.

6.1. Tuning of proportional–integral controller and model predictive controller

PI controllers are based on feedback sensor data and do not require a process model. However, the parameters of the PI controller must be tuned. The PI controller equations are as follows:

$$u = K_C \cdot \left[(y_{sp} - y) + \frac{1}{\tau_I} \cdot \int_0^t (y_{sp} - y)\, \mathrm{d}t' \right] \tag{13a}$$

$$u = I - I_s \tag{13b}$$

$$y_{sp} = C_{\mathrm{H}_2,\,sp} - C_{\mathrm{H}_{2,s}} \tag{13c}$$

$$y = C_{\mathrm{H}_2} - C_{\mathrm{H}_{2,s}} \tag{13d}$$

$$0\ \mathrm{A} \le u + I_s \le 70\ \mathrm{A} \tag{13e}$$

where u is the manipulated input, i.e., the current in deviation form, y is the output/state to be controlled, which is the hydrogen concentration in deviation form, y_{sp} is the setpoint for the hydrogen concentration that as chosen to be consistent with experimental steady-state data (although, in general, one can carry out steady-state optimization to calculate energy optimal set-points), and the subscript "s" denotes steady-state values. The actions of the PI controller are limited to be below 70 A of current, since currents higher than 70 A will be detrimental to the catalyst and cause coking. This limit is enforced by setting any current value calculated by the PI controller higher than 70 A to 70 A.

The model predictive controller takes the form of the following optimization problem:

$$\mathcal{J} = \min_u \int_{t_k}^{t_{k+N_h}} L(\hat{y}(t), u(t))\, \mathrm{d}t \tag{14a}$$

$$\text{s.t.} \quad \hat{x}(t) = ODE(x(t), u(t)) \tag{14b}$$

$$L(\hat{y}(t), u(t)) = A(\hat{y}(t) - y_{sp})^2 + B(u(t) - u_{sp})^2 \tag{14c}$$

$$t \in [t_k, t_{k+N_h}) \tag{14d}$$

$$|u(t_k) - u(t_{k-1})| \le 0.1\ \mathrm{A} \tag{14e}$$

$$0\ \mathrm{A} \le u + I_s \le 70\ \mathrm{A} \tag{14f}$$

where L is a cost function to be minimized over a prediction horizon of length N_h sampling periods using Eq. (14b), where ODE is the nonlinear dynamic process model derived in Section 4. The full state consisting of the 6 concentrations and the reactor temperature are represented by the state vector x, and $\hat{x}(t)$ is the full state prediction over the horizon using the ODE model computed by integrating the coupled system of 7 ODEs, while $\hat{y}(t)$ is the predicted hydrogen concentration in deviation form, i.e. $\hat{y}$ is the 4th column of $\hat{x}$ and the only state used in the cost calculation, but all 7 ODEs have to be integrated together due to their coupled nature. A and B are tunable weight parameters, and x_{sp} and u_{sp} are the set-points for the H_2 concentration and current, respectively. Similar to the PI controller, the optimization problem is aimed to produce outputs within the bounds of 0 and 70 A. However, since an MPC is inclined to drive the process very fast and hit the input bounds very early for a quick response, an additional constraint is placed that bounds consecutive current changes to a maximum of 0.1 A per second. This is also important for the catalyst morphology since a slow increase in current will not harm it.

The MPC will try to minimize the quadratic cost function over a horizon of 10 s. The estimated current set-point value (u_{sp}) is calculated by using the steady-state equations, which are obtained by equalizing the mass balance equations shown in Eq. (3) to 0. Here, the hydrogen concentration set-point is fixed, and the other gas concentrations and temperature are calculated using the process operating conditions. The current value corresponding to the calculated temperature is estimated from the correlation shown on Fig. 11. The weight parameters A and B

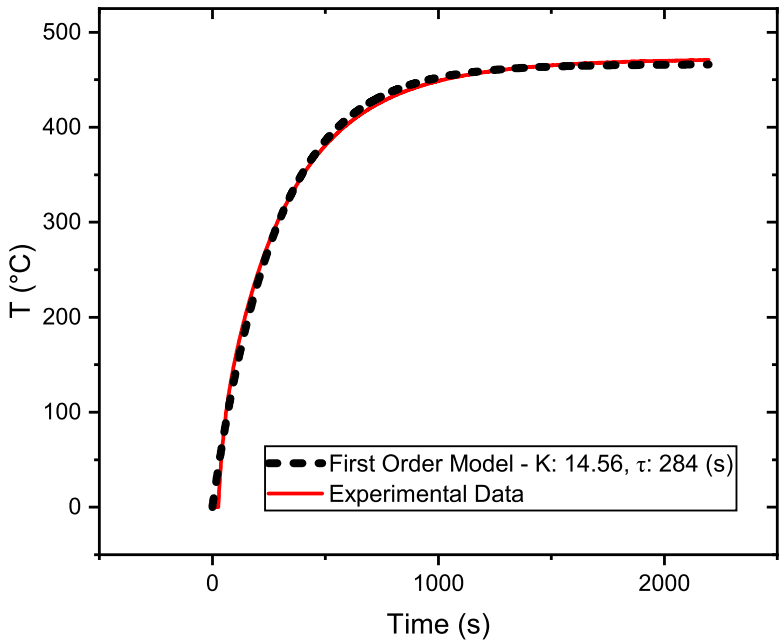

Fig. 12. Comparison of first order dynamic model with experimental observations.

for the quadratic cost function are tuned based on preliminary closed-loop simulations to get the most optimal responses based on the orders of magnitudes of inputs and outputs and finally taken to be 100 and 0.01, respectively. Qualitatively, the state penalty (A) was high, while the input penalty (B) was low, in order to speed up convergence to the setpoint and also to account for differences in magnitudes between the H2 concentration and the current. The MPC problem will be solved in real time in the future work on the experimental setup, thus requiring the MPC problem to be solvable within the sampling period of 1 s. To ensure this, the MPC optimization problem will be solved every second using a sequential quadratic programming (SQP) solver, which is a computationally-efficient solver (Boggs and Tolle, 1995). In the experimental implementation of the developed controllers, both MPC and PI, a sampling measurement frequency of 1 s for the process temperature, which is the key output variable that is controlled in this present work, may be used since every MPC calculation in the current work was completed in well under one second. This is consistent with the overall input–output process dynamics which are on the order of minutes.

All closed-loop simulations start from the same steady state that is described in Fig. 8 under constant temperature at 800 °C, constant current at 40 A and constant pressure at 1 bar. After the process reaches the steady state, it will remain there until the control action starts at the 100th second. The initial H_2 steady-state concentration will be 2.54 mol/m^3, and the controller is expected to drive the H_2 concentration to 4.5 mol/m^3. This number is 3 times the initial steady-state concentration and is a sufficiently large change to show that the controller is successful.

The MPC simulation results are shown in Fig. 13. After the set-point change is introduced at the 100th second, the controller starts to increase the temperature at 0.1 A per second to quickly drive the process towards the set-point. Around 300 s, the controller reaches its peak value at 60 A, and it can be seen that the process is very close to the set-point. After this point, the controller starts to reduce the current slowly to finalize the process evolution to the set-point, and the process settles at a steady state after around 600 s, where the temperature and current reach their respective steady states of 890 °C and 46 A. The MPC is solved quickly, drives the process output to the desired set-point without offset, and all the input constraints are respected.

Remark 9. The reaction reaches the initial steady state under 10 s. However, even with an MPC, it takes more than 220 s to reach a new steady state. The reason for this is that the temperature increase caused by the power supply has slower dynamic evolution compared to reaction dynamics.

In order to verify that the proposed MPC scheme is highly effective, it is compared with a PI controller. The PI controller is tuned to have no overshoot or oscillations. The parameters for the PI controller are taken to be $K_c = 0.12$, and $\tau_i = 20$. The comparison between the proposed PI controller and MPC is presented in Fig. 14. Both controllers succeed in driving the process to the set-point. It takes around 1300 s for the PI controller, while this duration was around 220 s for the MPC. The effectiveness of the MPC is due to the initial increase in the current input. Thus, the MPC is proven to be fast and efficient.

6.2. Disturbance rejection

In order to prove further effectiveness of the proposed MPC, it is necessary to demonstrate a robust performance against disturbances. One of the possible disturbances in the experimental setup is the steam flowrate. As explained in Section 3, there is a temperature control box that regulates the temperature of the bubblers. If the control box provides more heat, the steam flowrate going into the SMR reactor increases. Under normal circumstances, the steam-to-carbon ratio is arranged to flow 33 sccm of water vapor into the reactor. In case of a malfunction in the temperature control box, the amount of steam sent to the reactor might increase. In the presence of such a disturbance, the behavior of both the PI controller and MPC are examined.

The MPC performance against a 10% increase in steam feed flowrate is shown in Fig. 15. Compared to Fig. 13, it can be seen that the initial water steady state concentration is higher. Similar to the disturbance-free case, the controller gradually increases the current and then slowly decreases it to the set-point value as the concentration of H_2 gets closer to the set-point. However, in the +10% disturbance case, it is seen that the current is increased up to 61.93 A, which is also higher than the maximum current for the no-disturbance run. To quantify the differences in the dynamic responses with and without the disturbance in the steam box, we calculate the production of H_2 in terms of (standard) volumetric flow rate at the end of the run. For

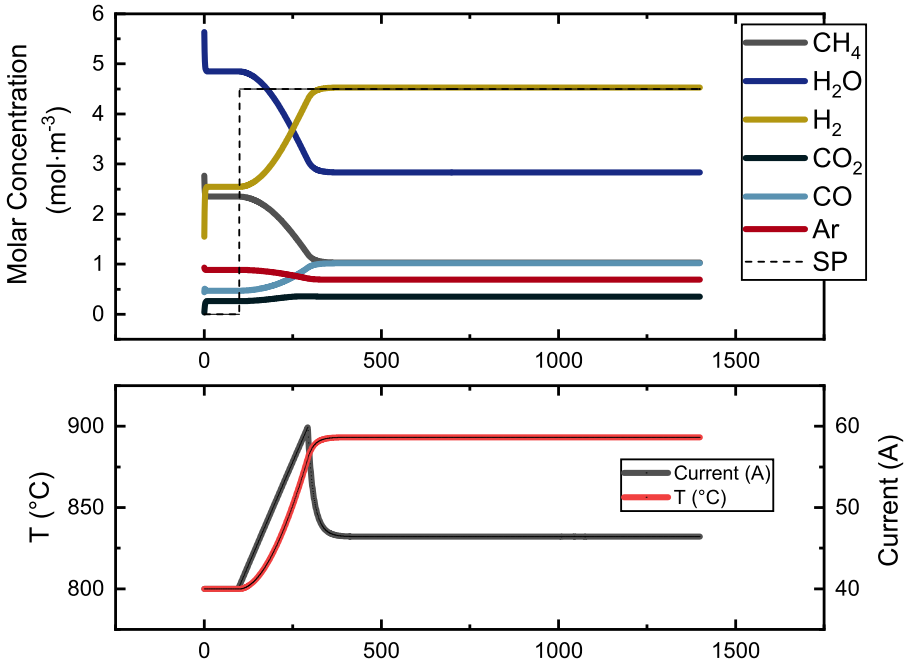

Fig. 13. Closed-loop response under MPC is fast and without offset while input constraints are respected.

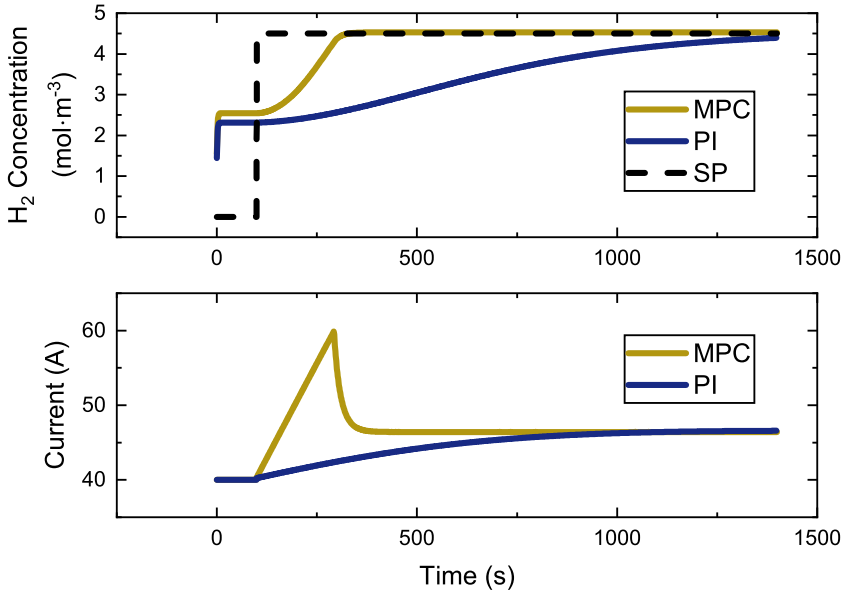

Fig. 14. Closed-loop response under MPC is superior to the one under PI control.

the case without disturbance, shown in Fig. 13, the final volumetric flow rate is 32.85 sccm, corresponding to a temperature of 893.38 °C and concentration of 4.5 mol/m^3. Under the disturbance, if the same temperature of 893.38 °C is maintained, the higher water vapor content in the inlet causes the steady-state concentration of H_2 to be reduced to 4.2 mol/m^3, yielding a reduced H_2 production rate of 31.57 sccm. However, under the MPC, using a higher peak current of 61.93 A, the final steady-state temperature is now adjusted to 913.56 °C to compensate for the excess water vapor in the feed. As a result, the hydrogen concentration once again reaches its setpoint of 4.5 mol/m^3, and the H_2 production increases to 35.59 sccm. This may be due to the extra water vapor in the feed stream decreasing the partial pressure of CH_4 and, consequently, the rate of the reforming reaction as per Eq. (2a). Thus, in order to reach the same level of H_2 production as the disturbance-free case, the controller needs to increase the heat provided to the system to boost the reaction rate of the reforming reaction.

The behavior of the PI controller is demonstrated in Fig. 16 against the 10% increase in the steam flowrate case. The same PI controller parameters are used as in Fig. 14. Although the PI controller manages to drive the process to the set-point, it takes longer than the MPC. The increase of steam flowrate requires more heat input, thus increasing the time to reach the set-point from 1300 s to 1900 s. On the other hand, the time required for the MPC to drive the process to the set-point under

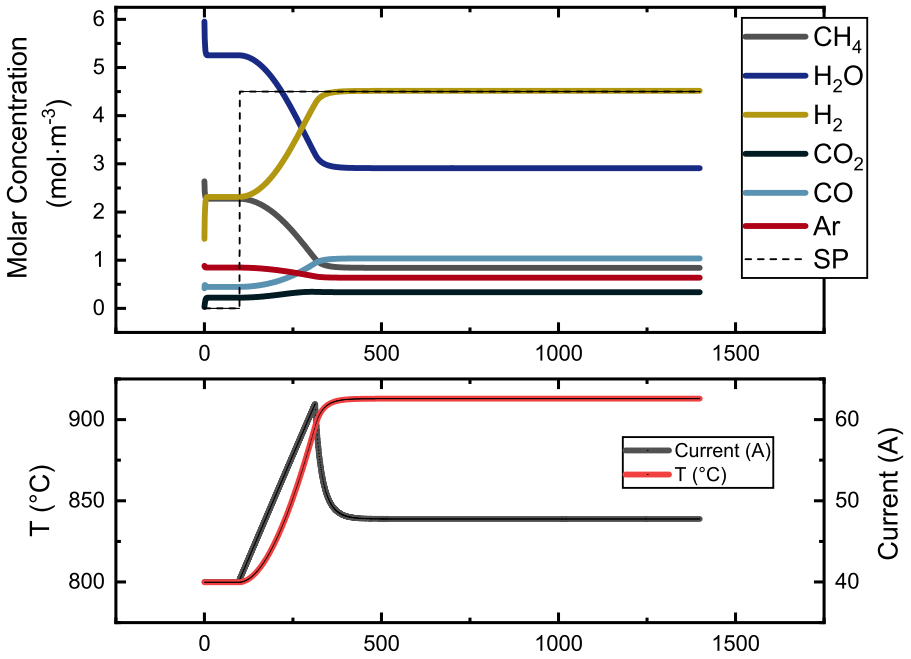

Fig. 15. Closed-loop response of the MPC under +10% disturbance in vapor feed flow rate.

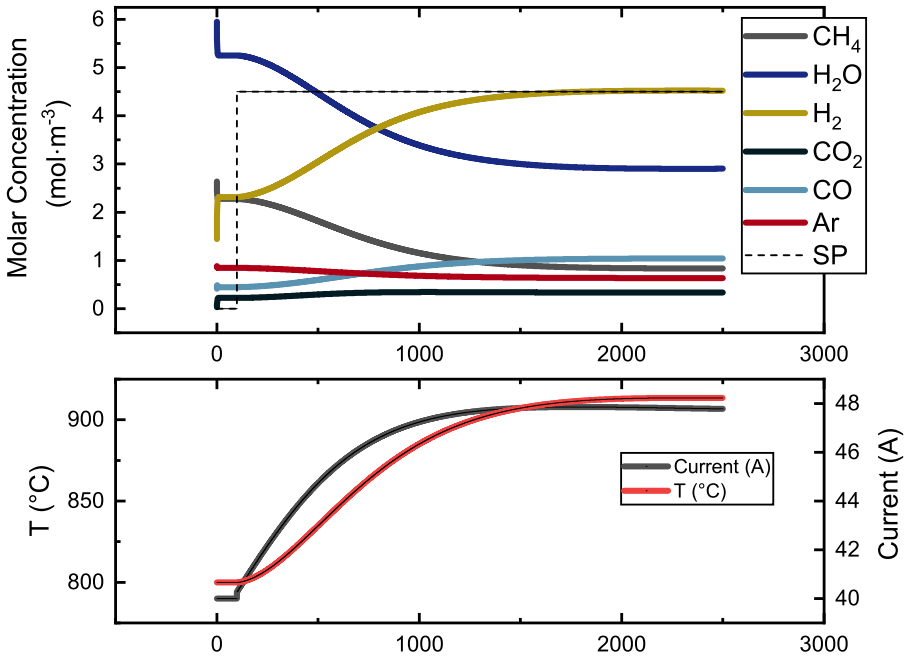

Fig. 16. Closed-loop response of the PI controller under +10% disturbance in vapor feed flow rate.

the disturbance had increased from 220 s to 370 s, showing that MPC is faster than the PI controller, and robust, in the disturbance case.

Remark 10. With respect to the essence of the comparison between the PI controller and the MPC, while the lower weight assigned to the control action contributes to the initial aggressiveness of the MPC, as long as all the constraints are satisfied and the state trajectory itself is satisfactory, the low input penalty is not a drawback of the MPC. The primary distinction in this comparison is that the PI controller, if it were tuned to be initially as aggressive as the MPC, would lead to overshoot and/or oscillations in the state, which the MPC avoids due to its predictive capabilities owing to the explicit use of a process model. The PI controller used was tuned extensively primarily to avoid overshoot and oscillations. Therefore, even if the MPC were to be compared to a PI controller that uses more aggressive control actions initially, the MPC would still outperform the PI controller in terms of the state trajectories due to the elimination of overshoot and oscillations. Therefore, the MPC is superior whether the PI controller is tuned to avoid overshoot/oscillations or it is tuned to be aggressive to match the speed of the MPC.

7. Conclusion

Steam methane reforming is the most common H_2 production method and can be made more sustainable through replacing fossil fuel based heating with electricity, and being able to control this process is

the key to maximizing the energy efficiency. The experimental setup for a joule heating SMR was modeled with first-principle nonlinear dynamic equations with parameters calculated using experimental data. Set-point tracking control was simulated under PI control and MPC. It was demonstrated that MPC leads to an optimal closed-loop response and is robust to disturbances. The MPC architecture built in this work will be implemented on the experimental electrified steam methane reforming reactor in a future work.

Declaration of competing interest

The authors declare that they have no known competing financial interests or personal relationships that could have appeared to influence the work reported in this paper.

Acknowledgments

We would like to gratefully acknowledge financial support from the U.S. Department of Energy, United States, through the Office of Energy Efficiency and Renewable Energy (EERE), under the Advanced Manufacturing Office Award Number DE-EE0007613. Financial support from the National Science Foundation, United States is also gratefully acknowledged.

References

Abbas, S.Z., Dupont, V., Mahmud, T., 2017. Kinetics study and modelling of steam methane reforming process over a NiO/Al_2O_3 catalyst in an adiabatic packed bed reactor. Int. J. Hydrogen Energy 42 (5), 2889–2903.

Boggs, P.T., Tolle, J.W., 1995. Sequential quadratic programming. Acta Numer. 4, 1–51.

Choudhary, N., Saraf, D., 1975. Hydrocracking: A review. Ind. Eng. Chem. Prod. Res. Dev. 14, 74–83.

Çıtmacı, B., Luo, J., Jang, J.B., Korambath, P., Morales-Guio, C.G., Davis, J.F., Christofides, P.D., 2022. Digitalization of an experimental electrochemical reactor via the smart manufacturing innovation platform. Digit. Chem. Eng. 5, 100050.

Fogler, H.S., 2005. Elements of Chemical Reaction Engineering (4th Edition), fourth ed. Prentice Hall.

Green, Jr., L., 1982. An ammonia energy vector for the hydrogen economy. Int. J. Hydrogen Energy 7, 355–359.

Hartig, O., Pérez, J., 2018. Semantics and complexity of GraphQL. In: Proceedings of the 2018 World Wide Web Conference. pp. 1155–1164.

IEA, 2023. Tracking Clean Energy Progress 2023. IEA Paris, France.

Lao, L., Aguirre, A., Tran, A., Wu, Z., Durand, H., Christofides, P.D., 2016. CFD modeling and control of a steam methane reforming reactor. Chem. Eng. Sci. 148, 78–92.

Latham, D.A., McAuley, K.B., Peppley, B.A., Raybold, T.M., 2011. Mathematical modeling of an industrial steam-methane reformer for on-line deployment. Fuel Process. Technol. 92, 1574–1586.

Liu, W., Zuo, H., Wang, J., Xue, Q., Ren, B., Yang, F., 2021. The production and application of hydrogen in steel industry. Int. J. Hydrogen Energy 46, 10548–10569.

Luo, J., Çıtmacı, B., Jang, J.B., Abdullah, F., Morales-Guio, C.G., Christofides, P.D., 2023. Machine learning-based predictive control using on-line model linearization: Application to an experimental electrochemical reactor. Chem. Eng. Res. Des. 197, 721–737.

Malerød-Fjeld, H., Clark, D., Yuste-Tirados, I., Zanón, R., Catalán-Martinez, D., Beeaff, D., Morejudo, S.H., Vestre, P.K., Norby, T., Haugsrud, R., et al., 2017. Thermo-electrochemical production of compressed hydrogen from methane with near-zero energy loss. Nat. Energy 2 (12), 923–931.

Mokheimer, E.M., Ibrar Hussain, M., Ahmed, S., Habib, M.A., Al-Qutub, A.A., 2015. On the modeling of steam methane reforming. J. Energy Resour. Technol. 137, 012001.

Nikolaidis, P., Poullikkas, A., 2017. A comparative overview of hydrogen production processes. Renew. Sustain. Energy Rev. 67, 597–611.

Perkin, R.M., 2000. Electrically generated heat. In: Ullmann's Encyclopedia of Industrial Chemistry. Wiley Online Library.

Ramachandran, R., Menon, R.K., 1998. An overview of industrial uses of hydrogen. Int. J. Hydrogen Energy 23 (7), 593–598.

Richard, D.M., 2021. Development and Testing of Two Lab-Scale Reactors for Electrified Steam Methane Reforming (M.Sc. thesis). UCLA.

Richard, D.M., 2023. A Smart Manufacturing Inspired Approach to Research in Electrochemistry Applied to Electrochemical Carbon Dioxide Reduction and Steam Methane Reforming (Ph.D. thesis). UCLA.

Safari, F., Dincer, I., 2020. A review and comparative evaluation of thermochemical water splitting cycles for hydrogen production. Energy Convers. Manage. 205, 112182.

Tanç, B., Arat, H.T., Baltacıoğlu, E., Aydın, K., 2019. Overview of the next quarter century vision of hydrogen fuel cell electric vehicles. Int. J. Hydrogen Energy 44, 10120–10128.

Tarhan, C., Çil, M.A., 2021. A study on hydrogen, the clean energy of the future: Hydrogen storage methods. J. Energy Storage 40, 102676.

Uddin, M.N., Nageshkar, V.V., Asmatulu, R., 2020. Improving water-splitting efficiency of water electrolysis process via highly conductive nanomaterials at lower voltages. Energy Ecol. Environ. 5, 108–117.

Ursua, A., Gandia, L.M., Sanchis, P., 2011. Hydrogen production from water electrolysis: Current status and future trends. Proc. IEEE 100 (2), 410–426.

Wei, J., Iglesia, E., 2004a. Isotopic and kinetic assessment of the mechanism of methane reforming and decomposition reactions on supported iridium catalysts. Phys. Chem. Chem. Phys. 6, 3754–3759.

Wei, J., Iglesia, E., 2004b. Isotopic and kinetic assessment of the mechanism of reactions of CH_4 with CO_2 or H_2O to form synthesis gas and carbon on nickel catalysts. J. Catal. 224, 370–383.

Wei, J., Iglesia, E., 2004c. Mechanism and site requirements for activation and chemical conversion of methane on supported Pt clusters and turnover rate comparisons among noble metals. J. Phys. Chem. B 108, 4094–4103.

Wei, J., Iglesia, E., 2004d. Reaction pathways and site requirements for the activation and chemical conversion of methane on Ru- based catalysts. J. Phys. Chem. B 108, 7253–7262.

Wei, J., Iglesia, E., 2004e. Structural and mechanistic requirements for methane activation and chemical conversion on supported iridium clusters. Angew. Chem. Int. Ed. 43, 3685–3688.

Wei, J., Iglesia, E., 2004f. Structural requirements and reaction pathways in methane activation and chemical conversion catalyzed by rhodium. J. Catal. 225, 116–127.

Wismann, S.T., Engbæk, J.S., Vendelbo, S.B., Bendixen, F.B., Eriksen, W.L., Aasberg-Petersen, K., Frandsen, C., Chorkendorff, I., Mortensen, P.M., 2019. Electrified methane reforming: A compact approach to greener industrial hydrogen production. Science 364 (6442), 756–759.

Wu, Z., Aguirre, A., Tran, A., Durand, H., Ni, D., Christofides, P.D., 2017. Model predictive control of a steam methane reforming reactor described by a computational fluid dynamics model. Ind. Eng. Chem. Res. 56, 6002–6011.

Xu, J., Froment, G.F., 1989. Methane steam reforming, methanation and water-gas shift: I. intrinsic kinetics. AIChE J. 35, 88–96.

Zecevic, N., Bolf, N., 2020. Advanced operation of the steam methane reformer by using gain-scheduled model predictive control. Ind. Eng. Chem. Res. 59, 3458–3474.